Controlled Synthesis of Nanomaterials using Reverse Micelles

Sonalika Vaidya, Jahangeer Ahmed, and Ashok K. Ganguli

Indian Institute of Technology Delhi, New Delhi-110 016

ABSTRACT

Monophasic nanosized oxides were synthesised mainly from metal oxalate nanorods obtained using the reverse micellar method. This paper focuses on the methodology to obtain important metal oxides like tin dioxide, cerium oxide (CeO_2), zirconia, and zinc oxide. The effect of oxidation state of the metal ion on the morphology of the oxalates was studied. Nanorods of zinc (II) oxalate (120 nm in dia and 600 nm in length) were obtained while spherical particles of size 4–6 nm were obtained for cerium (III) oxalate. The decomposition of these precursors at higher temperature led to the formation of their respective oxides. Mixture of nanorods and nanoparticles of CeO_2 was obtained while 3–4 nm sized ZrO_2 nanoparticles were obtained by thermal decomposition of zirconium oxalate precursor. The dielectric constant and loss were highly stable with frequency (at room temperature) for both ceria and zirconia nanoparticles. ZnO nanoparticles (55 nm sized) were obtained by the decomposition of zinc oxalate nanorods. Three peaks corresponding to free excitonic emission, free-to-bound, and donor-acceptor transitions were observed in the photoluminescence studies at 20 K for ZnO nanoparticles.

Keywords: Reverse micelles, monophasic nanosized oxides, metal oxalate nanorods, nano materials, synthesis of nanomaterials, top-down synthaesis, bottom-up synthesis

1. INTRODUCTION

Synthesis of nanomaterials by various routes have been developed to control the size of grains in these materials in the range of 1–100 nm. These materials show interesting properties compared to their bulk counterparts. Two approaches are being used for synthesising these materials, namely the top-down approach and the bottom-up approach. One of the bottom-up approches is followed where in the particles are formed as a result of atom by atom assembly. The method used is called the reverse micellar route, which involves a surfactant, co-surfactant, organic solvent, and aqueous solution mixed in a fixed proportion to form a stable, optically transparent system called microemulsion. These microemulsions contain tiny droplets of aqueous core stabilised by surfactant and co-surfactant dispersed homogeneously throughout the microemulsion. The size of these aqueous cores lies in the nano-regime. Thus, these aqueous cores act as nanoreactors which can be used to synthesise nanomaterials. This method has an advantage over other methods since they lead to homogeneous and monodisperse particles. Moreover, the morphology of the product can be controlled, through proper choice of the surfactant aggregates.

Various types of materials, viz., dielectric[1-3], magnetic[4,5], and optical[6], have been synthesised using the reverse micellar route. In addition, nanorods of a variety of transition metal oxalates[4,6,7] have

been successfully obtained. These nanorods of transition metal oxalates lead to the corresponding oxides of these metals, stabilised in different oxidation states, (by the decomposition of the transition metal oxalates)[4]. In this paper, some aspects of the synthesis of various nanomaterials and their properties are discussed.

The SnO_2 is used as a sensing material. It has a wide band gap (3.6 eV) and is a *n*-type semiconductor. It has its utility in various applications, viz., gas sensors[8], microelectronics[9], solar cells[10], and photoelectrochemistry[11] due to its unique conductance. It is also used as electrode material for lithium cells[12] and as photocatalysts[13]. Tin dioxide shows very high sensitivity towards reducing gases such as H_2, CO, hydrocarbon, and alcohol. Its sensitivity can be improved by increasing the surface area[8,14]. Song, *et al.* have used homogeneous precipitation method using urea from $SnCl_4$ solution to synthesise tin dioxide powders[15]. 25 nm SnO_2 nanoparticles were synthesised using water-in-oil microemulsion-assisted hydrothermal process by Chen[16], *et al.* Several other methods have also been used for the synthesis of SnO_2 nanoparticles such as sol-gel method[17,18], precipitation method[18,19], Pechini-citrate route[8,20], sputtering technique[21], chemical vapour deposition[22], surfactant mediated synthesis[23], and hydrothermal method[24]. A very important method to synthesise SnO_2 nanoparticles is the microemulsion method[12,25] in which reverse micelles are used as nanoreactors to limit the particle growth.

CeO_2 is a well known refractory material and has immense industrial importance. It has a high refractive index, strong adhesion, and stability towards high temperature, chemical attack, and mechanical abrasion. It is used for a variety of applications such as fuel cells[26], gas sensors[27], NO removal[28], counter electrodes in smart window devices, and humidity sensors[29]. Nanocrystalline CeO_2 particles with varied morphology, from square-like faces to hexagonal faces were formed when the temperature was increased, (hexagonal-shaped particles were also observed in an atmosphere with low oxygen content) have been synthesised earlier by precipitation method[30]. The size of the particle increased with temperature and decreased with increase in the oxygen content in the atmospheric condition.

Zirconia exists in three different structures, viz., monoclinic (thermodynamically most stable form, exists below 1170 °C), tetragonal (1170–2370 °C) and cubic (above 2370 °C). Zirconia is used as dielectric material in metal-oxide-metal capacitors for dynamic random access memory devices[31]. It has been used to replace Si in this case because of its high dielectric constant, thermal stability and large band gap. Tetragonal ZrO_2 shows good ionic conductivity and possesses high strength. Tetragonal ZrO_2 with minor impurity of the monoclinic phase has been synthesised via the sol-gel process from zirconyl oxalate[32].

ZnO is a wide band gap II–VI semiconductor due to which it is used as phosphor in field emissive displays[33,34], in cathodoluminescent devices[35], and dye-sensitised solar cells (DSSCs). It is used as an alternative to TiO_2 for solar cell application [36]. ZnO also finds a wide variety of applications in varistors[37]. A number of synthetic routes have been employed to synthesise ZnO nanoparticles, like sol-gel chemistry[38-42], spray pyrolysis[43], metal-organic chemical vapour deposition[44,45], cathodic electro-deposition,[46,47] and plasma pyrolysis[48].

2. EXPERIMENTAL

Two processes were used for synthesis of tin dioxide nanoparticles. In process I, two microemulsions I and II were used[49]. A colourless transparent solution was obtained after mixing the two microemulsions under constant stirring. $NaOH$ solution (0.1 M) was added to the resulting solution till the nucleation takes place and stirred overnight on a magnetic stirrer. The resulting precipitate was separated from the surfactant and apolar solvent by centrifugation and washing it with 1:1 mixture of methanol and chloroform. The precipitate was dried in an oven at 60 °C for 2 h to obtained SnO_2 powder. In process II, the SnO_2 nanoparticles were synthesised using aqueous NH_3 as the precipitating agent. The composition of the microemulsion was same as used in process I except that microemulsion II contained 0.1 M solution of NH_3 (25 %) instead of ammonium oxalate. The two microemulsions were mixed and stirred overnight. The resulting precipitate was washed as given above. The precipitate was

dried in an oven at 60 °C for 2 h. Monophasic SnO_2 nanoparticles were formed by heating the precursor in air at 500 °C for 5 h.

CeO_2 nanoparticles were synthesised by decomposing cerium oxalate precursor at 500 °C. The methodology followed was the reverse micellar (microemulsion) route with CTAB (cetyl trimethyl ammoniumbromide) as the surfactant[3]. For the synthesis of cerium oxalate precursor two different microemulsions, one containing cerium nitrate hexahydrate and the other containing ammonium oxalate, were slowly mixed and stirred for 15 h. The centrifuged product was washed with 1:1 mixture of chloroform and methanol and dried at room temperature. The product was decomposed at 500 °C for 6 h to obtain CeO_2.

ZrO_2 nanoparticles were also obtained by the thermal decomposition of zirconium oxalate. The procedure followed for the synthesis of zirconium oxalate was same as discussed for the synthesis of cerium oxalate. The two microemulsions contained aqueous solution of zirconyl oxychloride and ammonium oxalate, respectively. The precursor was decomposed at 500 °C for 6 h to obtain ZrO_2 nanoparticles. Effect of temperature on the structural transformation was studied by further heating the oxides at higher temperatures.

Zinc oxalate precursor was prepared using the reverse micellar route by a similar methodology as above. Microemulsion I contained zinc nitrate solution while microemulsion II contained ammonium oxalate solution. The two microemulsions were slowly mixed and stirred overnight. The centrifuged product was then washed with 1:1 chloroform/methanol mixture to remove the surfactant and and dried in an oven at 120 °C for 1 h. Zinc oxalate nanorods were heated at 450 °C for 6 h to obtain nanoparticles[6] of ZnO.

The compounds were characterised using powder x-ray diffraction (PXRD), dynamic light scattering (DLS), FTIR spectroscopy, transmission electron microscopy (TEM), scanning electron microscopy (SEM), and thermogravimetric/differential thermal analysis (TG/DTA). The characteristic properties such as photoluminescence (PL) for ZnO and dielectric properties for CeO_2 and ZrO_2 were also studied.

The PXRD studies were carried out on a Bruker D8 Advance diffractometer with Ni filtered $Cu\ K\alpha$ radiation with a scan speed of 1s and scan step of 0.05 °. The particle size was determined from the x-ray line broadening using Scherrer's Formula[50] [t = 0.9 λ/ ($B \cos \theta$)], where, t is the diameter of the particle, λ is the wavelength of $Cu\ K\alpha$ radiation (1.5418 Å) and B is the line broadening which is calculated by the Warren's formula[51,52]; $B^2 = (B_M{}^2 - B_S{}^2)$ where B_M is the full width at half maximum of the sample and B_S is the full width at half maximum of the standard quartz with a grain size of around 2 μm. The TGA/DTA experiments were carried out on Perkin Elmer Pyris Diamond TGA/DTA system on well ground samples in flowing nitrogen with a heating rate of 10 °C/min.

The light-scattering experiments were performed on a particle size analyser, model nano ZS90 (Malvern Instruments, UK). A He-Ne laser with a power of 4 mW was used as a light source. All the measurements were carried out at a scattering angle of 90° and at 25 °C, which was controlled by means of a thermostat. A dilute solution of the sample was prepared by dispersing the powder in water followed by ultrasonic treatment for 10 min. The IR studies were carried out on a Nicolet Protege 460 FTIR spectrometer. The data was recorded (with KBr disk) in the range of 400–4000 cm^{-1}. The SEM studies were carried out on Carl Zeiss EVO 50 WDS electron microscope.

The TEM studies were carried out using the Tecnai-20 G2 TEM. The TEM specimens were prepared by dispersing the powder in acetone by ultrasonic treatment, dropping onto a porous carbon film supported on a copper grid, and then dried in air. Mössbauer measurements for SnO_2 were carried out at room temperature with a conventional system operating in constant acceleration mode[49]. Dielectric measurements were carried on disks of CeO_2 nanoparticles sintered at 800 °C and 1000 °C and ZrO_2 nanoparticles sintered at 1000 °C The measurements were carried out using Hewlett Packard 4284L multifrequency LCR meter in the range of 50 Hz to 500 kHz. For PL studies on ZnO, the samples were housed in optical cryostat with front surface excitation and emitted radiation was collected for PL spectroscopy[6].

3. RESULTS AND DISCUSSION

3.1 SnO_2 Nanoparticles

The PXRD patterns of SnO_2 nanoparticles[49], obtained by process I (experimental section) is shown in Figs 1(a) and 1(b). All the reflections in the pattern could be indexed on the basis of a tetragonal cell (cassiterite) reported for SnO_2 (JCPDS # 21–1250). Particles with a crystallite size of 3–4 nm (60 °C) and 12 nm (500 °C) were obtained from the x-ray line broadening studies. Some agglomeration could be seen in the TEM micrograph of the samples heated at 60 °C (Fig. 2(a) and 500 °C (inset of Fig. 2(a). The grain size was found to be 70 nm (60 °C) and 150 nm (500 °C). The XRD pattern of the powder sample obtained by using NH_3 (process II) at 500 °C for 5 h is shown in Fig. 1(c). The particles were found to be 6–8 nm from TEM studies (Fig. 2(b)) which matches with the crystallite size calculated by the Scherrer's equation. Dynamic light scattering studies (Inset of Figs. 2(a) and 2(b)) show the uniform particle size distribution of the samples. However, the size is much larger (80–100 nm) than obtained by x-ray line broadening studies (5–8 nm) or by TEM. This may be due to aggregation of the particles in water during the DLS measurement. It may be noted that gas sensing properties are preferred on grains with 3–4 nm as grains less than 6 nm in dia as they have high sensitivity[53].
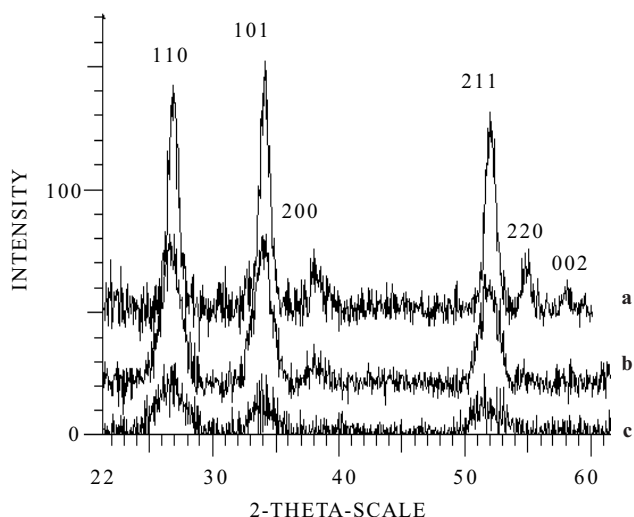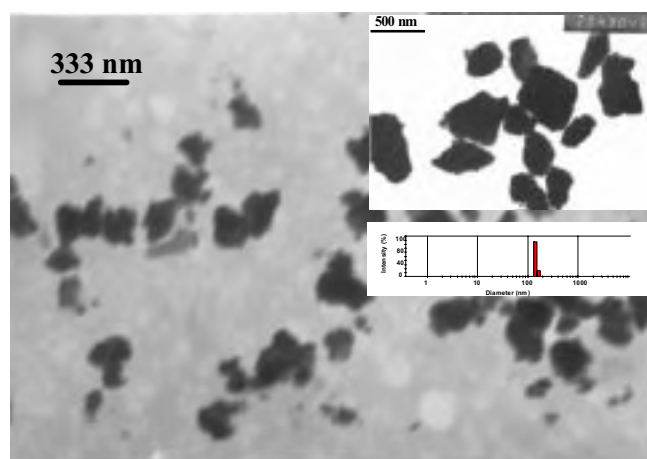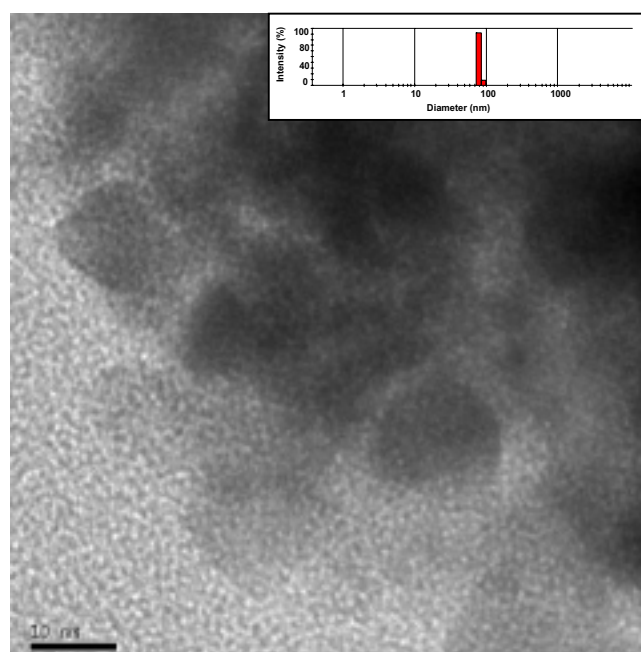

(a)

(b)

Figure 2. TEM micrograph of SnO_2 obtained by: (a) process I (60 °C), (Inset: micrograph of SnO_2 obtained by process I calcined at 500 °C and the size distribution plot obtained by the DLS studies, and (b) process II calcined at 500 °C (Inset: size distribution plot obtained by the DLS studies).

FTIR studies of SnO_2 shows peaks at ~3341 cm^{-1} and ~1630 cm^{-1} corresponding to the stretching vibration of -OH group and the bending vibration of adsorbed molecular water, respectively[54]. Stretching vibrations of Sn-O is indicated by a strong band at 633 cm^{-1}. This indicates that SnO_2 is well crystalline. The weak bands at 1393 cm^{-1} and 2921 cm^{-1} indicate the bending vibration of -CH_2 and stretching vibration

Figure 1. PXRD patterns of SnO_2 nanoparticles from: (a) process I (60 °C), (b) process I calcined at 500 °C, and (c) process II calcined at 500 °C.

of -*C-H* band[55] arising due to the surfactant molecules associated with SnO_2.

The Mössbauer spectrum (Fig. 3) of SnO_2 nanoparticles obtained by process II shows the SnO_2 nanoparticles show a very small isomer shift (0.04 mm/s) with respect to bulk SnO_2 along with a quadrupole splitting (QS) of 0.49 mm/s. Negligible QS (0.06 mm/s) is observed in bulk SnO_2. The small isomer shift is detected in the nanoparticles of SnO_2. This indicates an enhancement of *s*-electron density in comparison with the same in the bulk which indicates a small variation in the *Sn-O* bonding scheme in nanometric SnO_2. Lowering of the symmetry around the tin atoms is indicated by moderate QS (0.49 mm/s) in the nanometric SnO_2 which may be attributed to the oxygen vacancies[56]. Because of the characteristic broad line width of SnO_2, the changes in the isomer shift observed in the nano form are not clearly visible but the fitting gave the difference.

3.2 Cerium Oxide Nanoparticles

The PXRD studies of the product obtained after centrifugation of the microemulsion with *Ce*(III) ions and $C_2O_4^{2-}$ ions (dried at room temperature) show that all the reflections could be indexed on
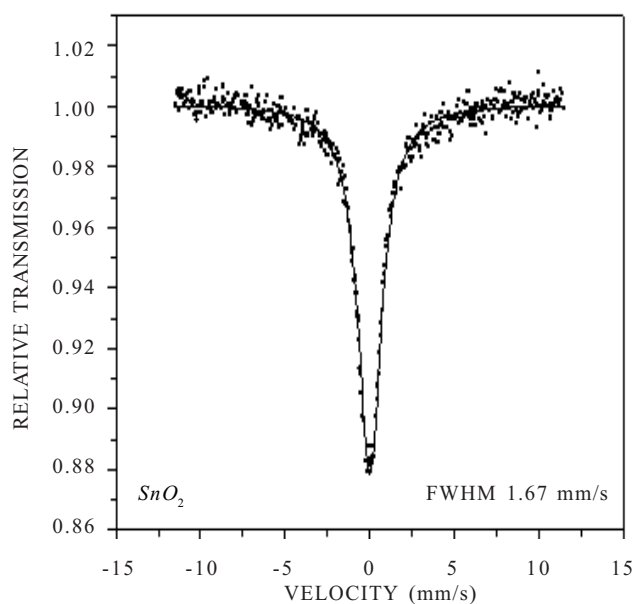

Figure 3. Mössbauer spectra of SnO_2 nanoparticles (obtained by process II).

the monoclinic cell of cerium oxalate decahydrate[3] (JCPDS No. 20–0268) (Inset of Fig. 4). The refined lattice parameters are $a = 11.311(3)$ Å, $b = 9.653(3)$ Å, $c = 10.390(3)$ Å and $\beta = 114.5°$. SEM studies (inset of Fig. 5(a)) show agglomerated cerium oxalate particles which are spherical in shape. HRTEM studies (Fig. 5(a)) show that the particle size obtained for the cerium oxalate precursor varied between
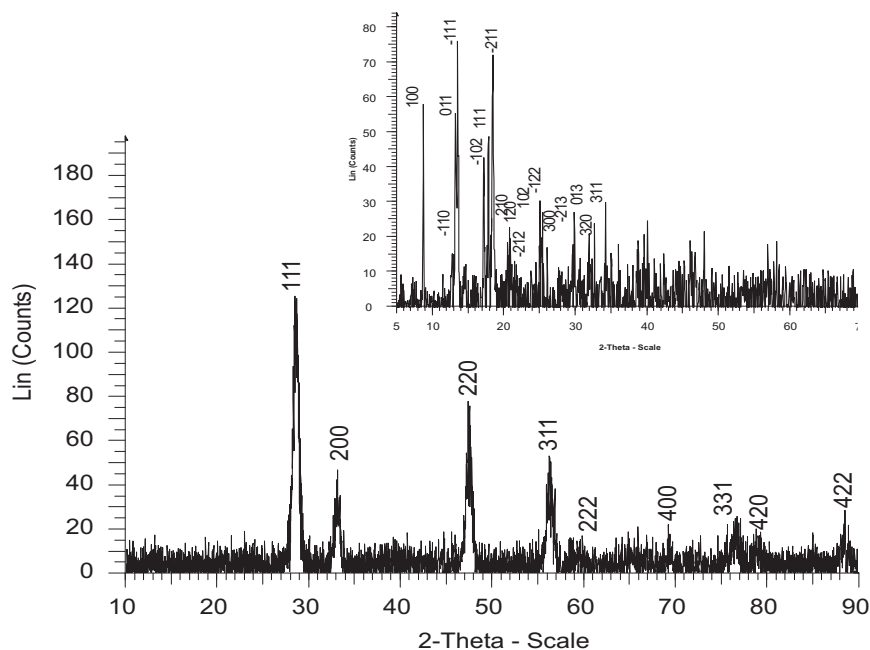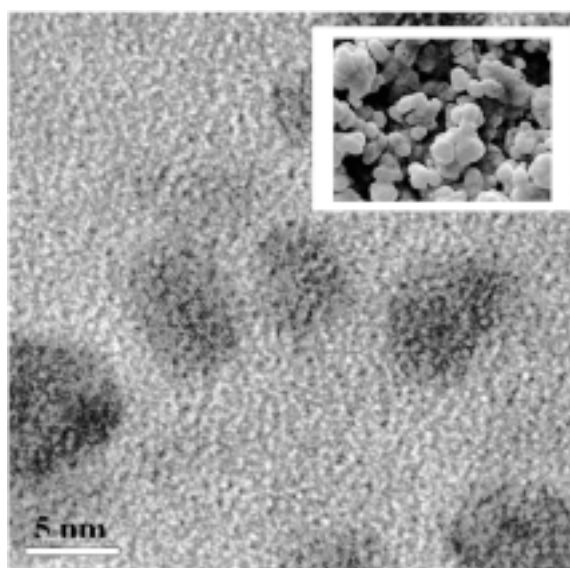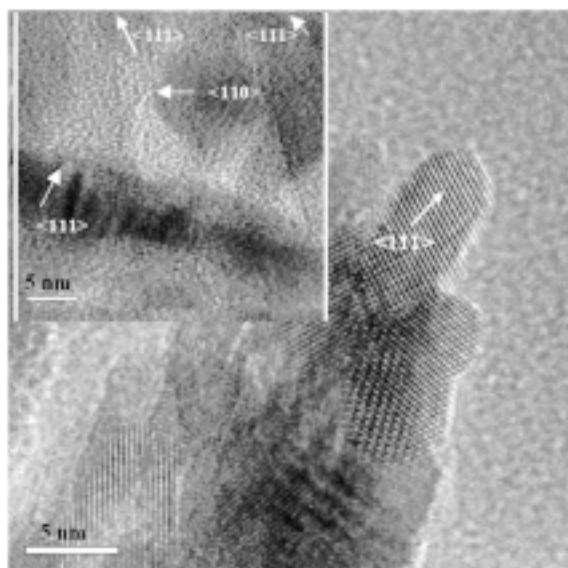

Figure 4. PXRD pattern of cubic cerium oxide (Inset: PXRD pattern of monoclinic cerium oxalate decahydrate).

(a)

(b)

Figure 5. **(a) TEM images for cerium oxalate synthesised at room temperature (Inset: SEM image for cerium oxalate synthesised at room temperature), and (b) HRTEM images of cerium oxide showing the growth of nanorods (Inset: Presence of nanorods and nanoparticle).**

4 nm to 6 nm. Note that cerium oxalate particles are spherical in shape where as the transition metal (*Cu*, *Ni*, *Mn,* and *Zn*) oxalates form as nanorods[4,6,7]. Note that the metals used, belong to the first row of transition series, and were all divalent whereas in this case *Ce* is trivalent. The divalent metal ion allows a 1:1 stoichiometry with the oxalate ion and

hence probably prefers to form a linear geometry between the oxalate and the divalent metal ion.

In the case of *Ce*, due to its trivalent oxidation state, a 1:1 stoichiometry is not possible with oxalate ion and this probably affects the formation of nanorods of cerium oxalate. The cerium oxalate precursor was decomposed at 500 °C to obtain nanocrystalline CeO_2 with a crystallite size of 15 nm. The PXRD pattern (Fig. 4) could be indexed on a cubic cell with *a* = 5.411(3) Å (JCPDS No. 81–0792). The HRTEM studies show the formation of both, particles (10 nm) and nanorods (7 nm in width and around 30 nm) in length for CeO_2 (inset of Fig. 5(b)). It seems that the particles are aggregating to form rods as observed in Fig. 5(b). An earlier study[57] reported the synthesis of spherical particles of cerium oxide (3.7 nm) (with no sign of any rods). Note that this study employed different microemulsion systems[57]. The PXRD pattern of CeO_2, taken after sintering at 800 °C and 1000 °C, showed the presence of cubic CeO_2.

The dielectric properties on sintered disks of CeO_2 at 800 °C show that the dielectric constant (~19 at 500 kHz) and dielectric loss (~ 0.11 at 500 kHz) were stable with frequency at room temperature. The dielectric constant was stable with temperature at 500 kHz, however the dielectric loss shows a minimum at 150 °C with a value of 0.028. The CeO_2 disks sintered at 1000 °C, the dielectric constant (15 at 500 kHz) and the loss (0.08 at 500 kHz) were found to be stable with frequency. The dielectric constant was stable with temperature, while the dielectric loss showed a constant value till 200 °C beyond which it rose sharply. An earlier report[58] on CeO_2 mentions a dielectric constant of 26. However, there was no mention of the grain size and the sintering temperature.

3.3. Zirconium Oxide Nanoparticles

The zirconium oxalate precursor, obtained using reverse micellar method was found to be amorphous[3]. The TGA/DTA studies for zirconium oxalate shows loss of one water molecule at 125 °C and a second loss at ~ 340 °C corresponding to the decomposition of the oxalate to form oxide. However, the oxide formed at this temperature was amorphous. The first endothermic peak in the DTA curve corresponds
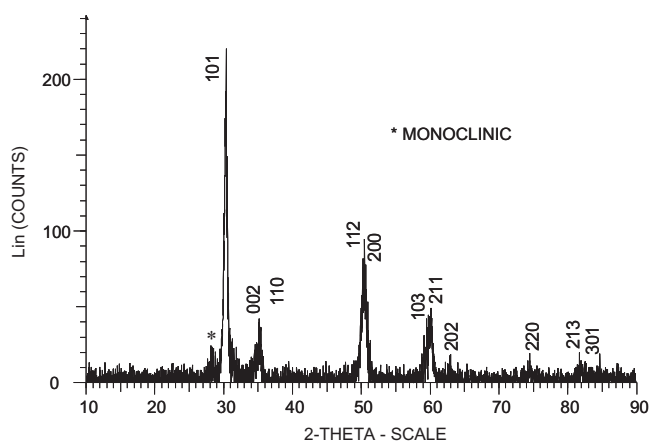
Figure 6. PXRD pattern for ZrO_2 obtained by the decomposition of zirconium oxalate and at 500 °C for 6 h.

Figure 7. TEM images for ZrO_2 synthesised by the decomposition of zirconium oxalate.

to loss of water molecule. The second peak in the DTA corresponds to the formation of oxide by the decomposition of its oxide. The peak in the DTA curve (at ~ 475 °C) could be related to a phase transition. No loss is seen in the TGA curve at 475 °C. Tetragonal ZrO_2 (crystallite size 12 nm) with 10 per cent impurity of monoclinic phase was obtained when the oxalate precursor was heated at 500 °C for 6 h (Fig. 6). The refined unit cell parameters were calculated for the tetragonal cell as a = 3.957(9) Å, c = 5.16(3) Å. The higher temperature tetragonal phase was successfully stabilised (tetragonal phase is normally stabilised between 1170–2370 °C) at low temperature. A minor amount of monoclinic phase appears on the decomposition of oxalate[59] (synthesised by the sol-gel method) in an earlier report on the synthesis of zirconia from zirconium oxalate. Further heating at 800 °C led to increase in the monoclinic phase and at 1000 °C only the pure monoclinic phase was obtained. TEM studies show the spherical grains of 3–5 nm (Fig. 7).

The dielectric constant of sintered disks (1000 °C) of ZrO_2 nanoparticles was found to be ~ 12 and the loss ~ 0.31 at 500 kHz. The dielectric constant and loss were highly stable with frequency at room temperature. Temperature variation studies show that the dielectric constant was stable after 100 °C, however the dielectric loss falls to ~ 0.03 at 100 °C from 0.31 at room temperature. Thompson[60], *et al.* reported that the dielectric constant for pure monoclinic zirconia is ~ 22 at 10 kHz.
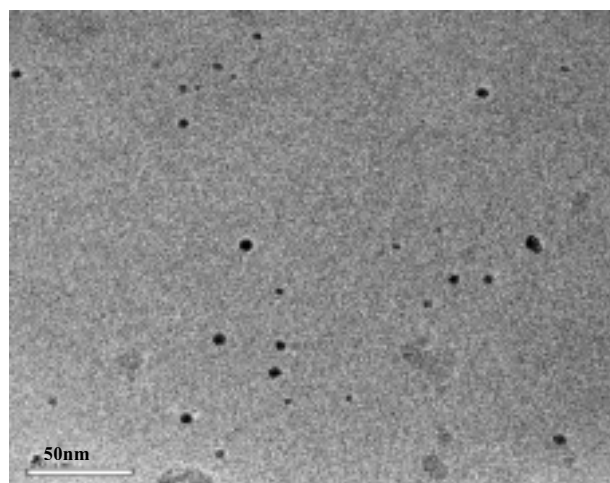
3.4 Zinc Oxalate Nanorods and Zinc Oxide Nanoparticles

The PXRD pattern of zinc oxalate dihydrate (Fig. 8) could be indexed on the basis of a monoclinic cell as reported earlier[6] (JCPDS # 25–1029). The TEM studies showed the formation of nanorods (120 nm in dia and 600 nm in length) of zinc oxalate dihydrate (inset of Fig. 8). AFM micrograph (Fig. 9) also show the formation of rods of zinc oxalate dihydrate nanorods. The size distribution plot from DLS studies gives an average size of ~ 375 nm (inset of Fig. 9). Zinc oxalate nanorods show a size distribution in the range of 200–500 nm. It is known that the DLS technique does not
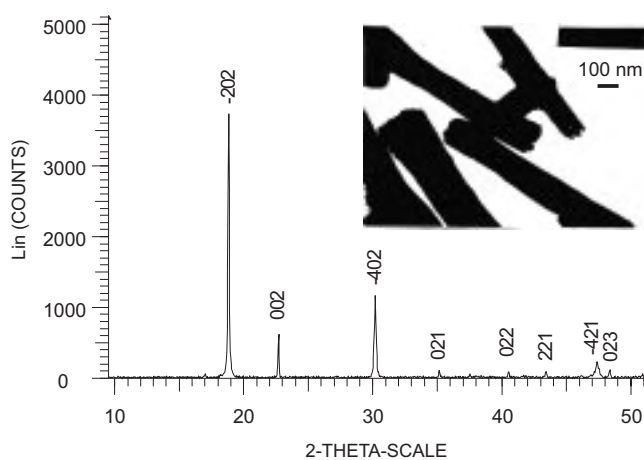

Figure 8. PXRD of zinc oxalate (Inset: TEM micrograph of the nanorods of zinc oxalate).

give the distribution of lengths or widths of the nanorods. It averages out the dimensions in the form of an equivalent sphere.

TGA of the oxalate precursor showed two weight losses. The first weight loss at 120 °C corresponded to loss of two water molecules. The second weight loss at around 400 °C led to the conversion of anhydrous zinc oxalate to zinc oxide. Two weight losses, corresponding to the weight losses in TGA studies, were also observed in the DTA studies. With these results the precursor was calcined at 450 °C for 6 h for the conversion of zinc oxalate to zinc oxide.

PXRD pattern of zinc oxide nanoparticles, with a crystallite size of 48 nm, is shown in Fig. 10. The pattern was indexed on the basis of a hexagonal cell with the refined lattice parameters of $a = 3.2498(4)$Å and $c = 5.209(1)$ Å.

Inset of Fig. 10 shows the TEM micrograph of the spherical particles of *ZnO* nanoparticles with an average grain size of 55 nm. A uniform size distribution of *ZnO* nanoparticles (40–100 nm) with an average size of 60 nm is obtained from DLS studies (Fig. 11). Detailed PL studies were carried out on these 55 nm *ZnO*. Three band edge transitions were observed in the deconvoluted PL spectra (Fig. 12) of *ZnO* nanoparticles. The first at 3.34 eV corresponded to free excitonic transition, the second at 3.04 eV corresponded to free-to-bound transitions and the third at 2.78 eV was observed due to donor-acceptor pair transition[61]. A weak peak at 2.5 eV was also observed which could be due to the chromium present in the quartz substrate. Strong PL intensity was observed from the sample which suggests excellent sample quality. However there is no quantum confinement effect as is normally present in 2–3 nm-sized nanoparticles[62,63] because the particle size of *ZnO* in this study is much larger (~55 nm).

The temperature dependence of the PL spectra is shown in the inset of Fig. 12. The PL intensity should decrease with increase in temperature due to thermal quenching of free excitons. However, in present work a non-monotonic temperature dependence of the excitonic spectra is observed, which could be due to exchange splitting of the excitonic level between threefold degenerate triplet
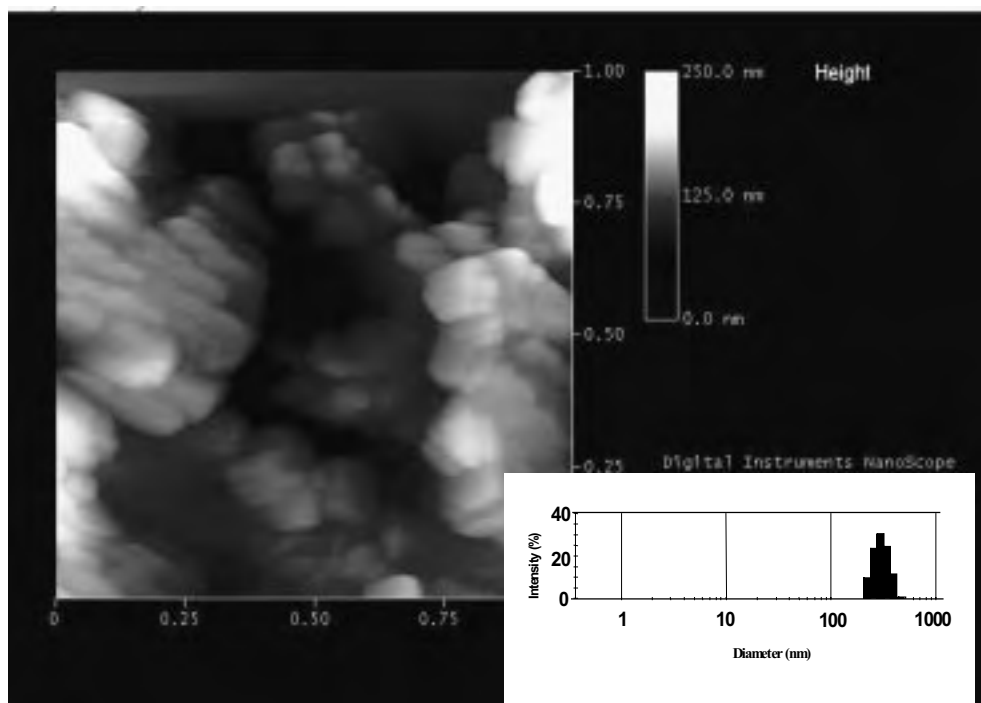

Figure 9. AFM micrograph of the nanorods of zinc oxalate. (Inset: Size distribution plot obtained by DLS study for nanorods of zinc oxalate).
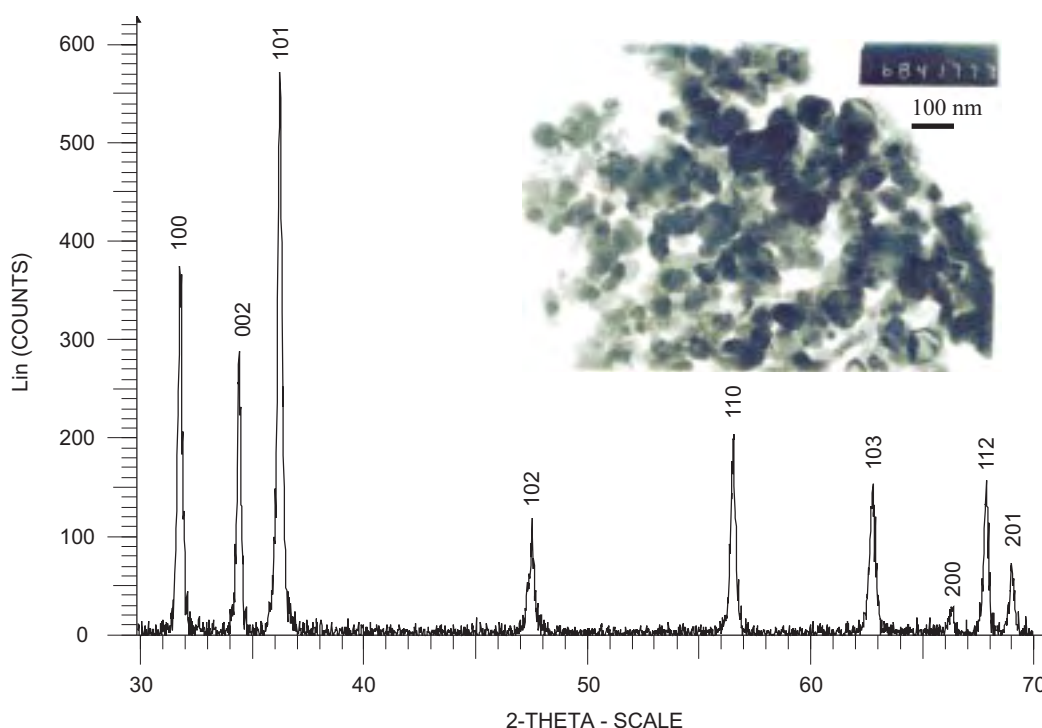
Figure 10. PXRD of zinc oxide nanoparticles (Inset: TEM micrograph of zinc oxide nanoparticles).
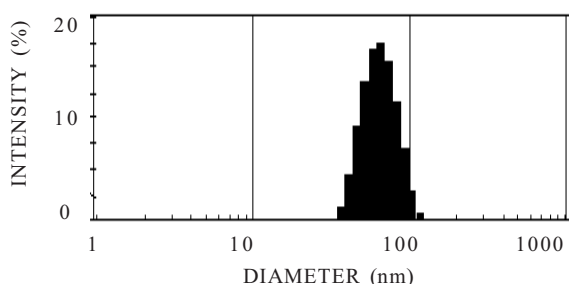

Figure 11. Size distribution plot for zinc oxide nanoparticles using DLS studies.

state and the higher singlet state. A similar observation of the dependence of PL intensity on temperature has been observed in porous silicon[64]. The radiative decay rate is small because at low temperature only the lower lying triplet state is occupied. This is because the optical transition from a pure triplet state is forbidden, but, due to spin-orbit interaction (mixes triplet and singlet states) the optical transition becomes allowed though with a very low quantum yield. At higher temperatures, the higher singlet state is occupied and the quantum yield of the optical transition increases and attains a maximum, but, further

increase in temperature leads to thermal quenching of the bound states resulting in the decrease of PL intensity.
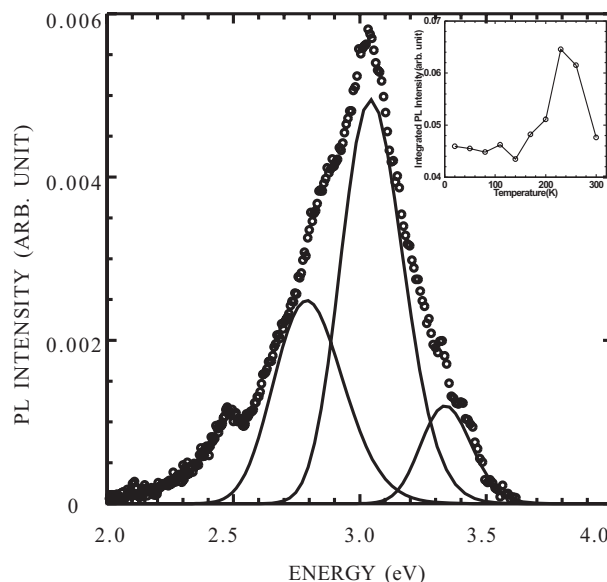

Figure 12. PL spectra at 20 K (empty circles). Three deconvoluted Gaussian peaks centered at 3.34 eV, 3.04 eV, and 2.78 eV are also shown (Inset: Integrated PL intensity plot versus temperature), connecting line is guide for eyes.

4. CONCLUSIONS

Nanorods of various transition metal oxalates and their corresponding oxide nanoparticles are synthesised using the reverse micellar route. The role of the oxidation state of the metal ion on morphology and size of particles were investigated. With different oxidation state of the metal ions, the morphology of the product changed. The oxalates were used as a precursor to synthesise oxide nanoparticles with variable oxidation states. The present work shows that this methodology is quite suitable to synthesise nanoparticles of different sizes (3–60 nm).

ACKNOWLEDGEMENTS

REFERENCES

1. Ahmad, T. & Ganguli, A.K. Reverse micellar route to nanocrystalline titanates ($SrTiO_3$, Sr_2TiO_4, and $PbTiO_3$): Structural aspects and dielectric properties. *J. Amer. Ceram. Soc.*, 2006, **89**, 1326-332.

2. Ahmad, T.; Kavitha, G.; Narayana, C. & Ganguli, A.K. Nanostructured barium titanate prepared through a modified reverse micellar route: Structural distortion and dielectric properties. *J. Mater. Res.,* 2005, **20**, 1415-421.

3. Vaidya, S.; Ahmad, T.; Agarwal, S. & Ganguli, A.K. Nanocrystalline oxalate/carbonate precursors of *Ce* and *Zr* and their decompositions to CeO_2 and ZrO_2 nanoparticles. *J. Amer. Ceram. Soc.*, 2007, **90**, 863-69.

4. Ahmad, T.; Ramanujachary, K.V.; Lofland, S.E. & Ganguli, A.K. Nanorods of manganese oxalate: A single source precursor to different manganese oxide nanoparticles (MnO, Mn_2O_3, Mn_3O_4). *J. Mater. Chem.*, 2004, **14**, 3406-410.

5. Ahmad, T.; Ramanujachary, K.V.; Lofland, S.E. & Ganguli, A.K. Magnetic and electrochemical properties of nickel oxide nanoparticles obtained by the reverse-micellar route. *Solid State Sciences,* 2006, **8**, 425-30.

6. Ahmad, T.; Vaidya, S.; Sarkar, N.; Ghosh, S. & Ganguli, A.K. Zinc oxalate nanorods: A convenient precursor to uniform nanoparticles of ZnO. *Nanotechnology*, 2006, **17,** 1236-240.

7. Ahmad, T.; Chopra, R.; Ramanujachary, K.V.; Lofland, S.E. & Ganguli, A.K. Nanorods of copper and nickel oxalates synthesised by the reverse micellar route. *J. Nanosci. Nanotech.*, 2005, **5**, 1840-845.

8. Niranjan, R.S.; Hwang, Y.K.; Kim, D.K.; Jhung, S.H.; Chang, J.S. & Mulla, I.S. Nanostructured tin oxide: Synthesis and gas-sensing properties. *Mater. Chem. Phys.,* 2005, **92**, 384-88.

9. Schiller, S.; Heisig, U.; Goedicke, K.; Bilz, H. & Steinfelder, K. Methods and applications of plasmatron high rate sputtering in microelectronics, hybrid microelectronics and electronics. *Thin Solid Films,* 1982, **92**, 81-98.

10. Lee, S.C.; Lee, J.H.; Oh, T.S. & Kim, Y.H. Fabrication of tin oxide film by sol–gel method for photovoltaic solar cell system. *Sol. Energy Mater. Sol. Cells,* 2003, **75**, 481-87.

11. Stergiopoulos, T.; Arabatzis, I.M.; Cachet, H. & Falaras, P. Photoelectrochemistry at SnO_2 particulate fractal electrodes sensitized by a ruthenium complex solid-state solar cell assembling by incorporating a composite polymer electrolyte. *J. Photochem. Photobiol. A Chem.*, 2003, **155**, 163-70.

12. Aurbach, D.; Nimberger, A.; Markovasky, B.; Levi, E.; Sominsky, E. & Gedanken, A. Nanoparticles of SnO produced by sonochemistry as anode materials for rechargeable lithium batteries. *Chemistry of Materials*, 2002, **14**, 4155-163.

13. Miyauchi, M.; Nikajima, A.; Watanabe, T. & Hasimoto, K. Photocatalysis and photoinduced hydrophilicity of various metal oxide thin films. *Chemistry of Materials*, 2002, **14**, 2812-816.

14. Li, G.–J. & Kawi, S. High-surface-area SnO_2: A novel semiconductor-oxide gas sensor. *Materials Letters,* 1998, **34**, 99-102.

15. Song, K.C. & Kang, Y. Preparation of high surface area tin oxide powders by a homogeneous precipitation method. *Materials Letters*, 2000, **42**, 283-89.

16. Chen, D. & Gao, L. Novel synthesis of well-dispersed crystalline SnO_2 nanoparticles by water-in-oil microemulsion-assisted hydrothermal process. *J. Colloid Interface Sci.,* 2004, **279**, 137-42.

17. Korosi, L.; Papp S.; Meynen V.; Cool P.; Vansant E.F. & Dekany I. Preparation and characterization of SnO_2 nanoparticles of enhanced thermal stability: The effect of phosphoric acid treatment on $SnO_2 \cdot nH_2O$. *Colloids & Surfaces A,* 2005, **268**, 147-54.

18. Zhang, J. & Gao, L. Synthesis and characterisation of nanocrystalline tin oxide by sol-gel method. *J. Solid State Chem.,* 2004, **177**, 1425-430.

19. Song, K.C. & Kim, J.H. Synthesis of high surface area tin oxide powders via water-in-oil microemulsions. *Powder Technology*, 2000, **107**, 268-72.

20. Pechini M.P. US patent 3 (1967) 697.

21. Ma, J.; Wang, Y.; Ji, F.; Yu, X. & Ma, H. UV–violet photoluminescence emitted from SnO_2:Sb thin films at different temperature. *Materials Letters*, 2005, **59**, 2142-145.

22. Calestani, D.; Lazzarini, L.; Salviati, G. & Zha, M. Morphological , structural, and optical study of quasi-1D SnO₂ nanowires and nanobelts. *Cryst. Res. Technol.*, 2005, **40**, 937.

23. Wang, Y.–D.; Ma, C.–L.; Sun, X.–D. & Li, H.–D. Synthesis of mesostructured SnO_2 with CTAB and hydrous tin chloride. *Materials Letters,* 2001, **51**, 285-88.

24. Guo, C.; Cao, M. & Hu, C. A novel and low-temperature hydrothermal synthesis of SnO_2 nano-rods. *Inorg. Chem. Commun.,* 2004, **7**, 929-31.

25. Song, K.C. & Kim, J.H. Preparation of nanosize tin oxide particles from water-in-oil microemulsions. *J. Colloid Interface Sci.*, 1999, **212**, 193-96.

26. Steele, B.C.H. & Heinzel, A. Materials for fuel-cell technologies. *Nature*, 2001, **414**, 345-52.

27. Garzon, F.H.; Mukundan, R. & Brosha, E.L. Solid-state mixed potential gas sensors: Theory, experiments and challenges. *Solid State Ionics*, 2000, **136/137**, 633-38.

28. Dimonte, R.; Fornasiero, P.; Graziani M. & Kašpar, J. Oxygen storage and catalytic NO removal promoted by CeO_2-containing mixed oxides. *J. Alloys Compound*, 1998, 275-77, 877-85.

29. Elidrissi, B.; Addou, M.; Regragui, M.; Monty, C.; Bougrine, A. & Kachouane, A. Structural and optical properties of CeO_2 thin films prepared by spray pyrolysis. *Thin Solid Films*, 2000, **379**, 23-27.

30. Chen, H.I. & Chang, H.Y. Synthesis of nanocrystalline cerium oxide particles by the precipitation method. *Ceramics International*, 2005, **31**, 795-802.

31. Chang, J.P. & Lin, Y.S. Highly conformal ZrO_2 deposition for dynamic random access memory application. *J. Appl. Phys.*, 2001, **90**, 2964-969.

32. Etienne, J.; Larbot, A.; Julbe, A.; Guizard, C. & Cot, L. A microporous zirconia membrane prepared by the sol-gel process from zirconyl oxalate. *J. Membrane Sci.*, 1994, **86**, 95-102.

33. Vanheusden, K.; Saeger, C.H.; Warren, W.L.; Tallant, D.R. & Voight, J.A. Correlation between photoluminescence and oxygen vacancies in ZnO phosphors. *Appl. Phys. Lett.,* 1996, **68**, 403-05.

34. Vanheusden, K.; Warren, W.L.; Saeger, C.H.; Tallant, D.R. & Voight, J.A. Mechanisms behind

green photoluminescence in *ZnO* phosphor powders. *J. Appl. Phys.*, 1996, **79**, 7983-990.

35. Bachir, S.; Sandouly, C.; Kossanyi, J. & Ronfard-Haret, J.C. Rare earth-doped polycrystalline zinc oxide electroluminescent ceramics. *J. Phys. Chem. Solids,* 1996, **57**, 1869-879.

36. Bu Burnside, S.; Winkel, S.; Brooks, K.; Shklover, V.; Gratzel, M.; Hinsch, A.; Kinderman, R.; Bradbury, C.; Hagfeldt, A. & Pettersson, H. Deposition and characterisation of screen-printed porous multilayer thick film structures from semiconducting and conducting nanomaterials for use in photovoltaic devices. *J. Mater. Sci.: Mater. Electronics*, 2000, **11**(4), 355-62.

37. Gupta, T.K. Application of zinc oxide varistors. *J. Amer. Ceram. Soc.*, 1990, **73,** 1817-840.

38. Hoyer, P. & Wellar, H. Size-dependent redox potentials of quantized zinc oxide measured with an optically transparent thin layer electrode. *Chem. Phys. Lett.*, 1994, **221**, 379-84.

39. Bahnemann, D.W.; Kormann, C. & Hoffmann, M.R. Preparation and characterization of quantum size zinc oxide: A detailed spectroscopic study. *J. Phys. Chem.,* 1987, **91**, 3789-798.

40. Haase, M.; Wqeller, H. & Henglein, A. Photochemistry and radiation chemistry of colloidal semiconductors. 23. Electron storage on zinc oxide particles and size quantization. *J. Phys. Chem.,* 1988, **92**, 482-87.

41. Sakohara, S.; Tickanen, L.D. & Anderson, M.A. Luminescence properties of thin zinc oxide membranes prepared by the sol-gel technique: Change in visible luminescence during firing. *J. Phys. Chem.*, 1992, **96**, 11086-1091.

42. Spanhel, L. & Anderson, M.A. Semiconductor clusters in the sol-gel process: Quantized aggregation, gelation, and crystal growth in concentrated zinc oxide. *J. Amer. Chem. Soc.*, 1991,**113**, 2826-833.

43. De Merchant, J. & Cocivera, M. Preparation and doping of zinc oxide using spray pyrolysis. *Chemistry of Materials*, 1995, **7**, 1742-749.

44. Roth, A.P. & Williams, D.F. Properties of zinc oxide films prepared by the oxidation of diethylzinc. *J. Appl. Phys.*, 1981, **52**, 6685-692.

45. Maruyama, T. & Shionoya, J. Zinc oxide thin films prepared by chemical vapor deposition from zinc acetate. *J. Mater. Sci. Lett.*, 1992, **11**, 170-72.

46. Izaki, M. & Omi, T. Transparent zinc oxide films prepared by electrochemical reaction. *Appl. Phys. Lett.*, 1996, **68**, 2339-340.

47. Peulon, S. & Lincot, D. Cathodic electrodeposition of dense or open-structured zinc oxide films from aqueous solution. *Advances in Materials,* 1996, **8**, 166-70.

48. Lin, Y.; Tang, Z. & Zhang, Z. Preparation of nanometer zinc oxide powders by plasma pyrolysis technology and their applications. *J. Amer. Ceram. Soc.*, 2000, **83**, 2869-871.

49. Ahmed, J.; Vaidya S.; Ahmad, T.; Devi P.S.; Das, D. & Ganguli, A.K. Tin dioxide nanoparticles: Reverse micellar synthesis and gas sensing properties. *Mater. Res. Bull.,* 2008, **43**, 264-71.

50. Birks, L.S. & Friedman, H. Particle size determination from x-ray line broadening. *J. Appl. Phys.,* 1946, **17**, 687-92.

51. Warren, B.E. & Averbach B.L. The effect of cold-work distortion on x-ray patterns. *J. Appl. Phys.,* 1950, **21**, 595-99.

52. Warren, B.E. & Averbach, B.L. The separation of cold-work distortion and particle size broadening in x-ray patterns. *J. Appl. Phys.,* 1952, **23**, 497.

53. Wang, Y.; Jiang, X. & Xia, Y. A solution-phase, precursor route to polycrystalline *SnO₂* nanowires that can be used for gas sensing under ambient conditions. *J. Amer. Chem. Soc.,* 2003, **125**, 16176-6177.

54. Sibu, C.P.; Kumar, S.R.; Mukundan, P. & Warrier, K.G.K. Structural modifications and associated properties of lanthanum oxide doped sol-gel

nanosized titanium oxide. *Chemistry of Materials*, 2002, **14**, 2876-881.

55. MacPhail, R.A.; Strauss, H.L. & Snyder, R.G. C-H stretching modes and the structure of n-alkyl chains. 2. Long, All-Trans Chains. *J. Phys. Chem.,* 1984, **88**, 334-41.

56. Pereira, A.G.; Porto, A.O.; de Lima, G.M.; Siebald, H.G.L. & Ardission, J.D. 119Sn Mossbauer spectroscopic study of nanometric tin dioxide powders prepared by pyrolysis of organotin oxides. *Solid State Communications,* 2003, **127**, 223-27.

57. Sathyamurthy, S.; Leonard, K.J.; Dabestani, R.T. & Paranthaman, M.P. Reverse micellar synthesis of cerium oxide nanoparticles. *Nanotechnology,* 2005, **16**, 1960-964.

58. Logothetidis, S.; Patsalas, P.; Evangelou, E.K.; Konofaos, N.; Tsiaoussis, I. & Frangis, N. Dielectric properties and electronic transitions of porous and nanostructured cerium oxide films. *Mater. Sci. Engg. B*, 2004, **109**, 69-73.

59. Etienne, J.; Larbot, A.; Julbe, A.; Guizard, C. & Cot, L. A microporous zirconia membrane prepared by the sol-gel process from zirconyl oxalate. *J. Membrane Sci.*, 1994, **86**, 95-102.

60. Thompson, D.P.; Dickins, A.M. & Thorp, J.S. The dielectric properties of zirconia. *J. Mater. Sci.*, 1992, **27**, 2267-271.

61. Srikant, V. & Clarke, D.R. On the optical band gap of zinc oxide. *J. Appl. Phys.*, 1998, **83,** 5447-451.

62. Haase, M.; Weller, H. & Henglwin, A. Photochemistry and radiation chemistry of colloldal semiconductors. 23. Electron storage on *ZnO* particles and size quantization. *J. Phys. Chem.,* 1988, **92**, 482-87.

63. Guo, L.; Yang, S.; Yang, C.; Yu, P.; Wang, J.; Ge, W. & Wong, G.K.L. Highly monodisperse polymer-capped *ZnO* nanoparticles: Preparation and optical properties. *Appl. Phys. Lett.,* 2000, **76**, 2901-903.

64. Calcott, P.D.J.; Nash, K.J.; Canham, L.T.; Kane, M.J. & Brumhead, D. Identification of radiative transitions in highly porous silicon. *J. Phys.: Condens. Matter*, 1993, **5**, L91-L98.

Contributors

Ms Sonalika Vaidya obtained her BSc (Hons) Chemistry from University of Delhi in 2002, and MSc (Chemistry) from Indian Institute of Technology Delhi, New Delhi, in 2004 after which she joined for PhD and is currently working on core shell nanostructures.

Mr Jahangeer Ahmed obtained his BSc from KLDAV Degree College, Roorkee, (affiliated to Choudhary Charan Singh University, Meerut) in 2001 and MSc (Chemistry) from IIT Roorkee in 2003. He is persuing his PhD from IIT Delhi on bimetallic nanosized alloys obtained from reverse micellar method and their properties.

Prof Ashok Kumar Ganguli obtained his PhD from Indian Institute of Science, Bangalore, in 1990 in the area of (solid state chemistry) of thallium superconductors for which he got the *Sudborough Medal*. He worked at Ames Laboratory, Iowa State University, USA in the area of intermetallic compounds and zintl phases. He is working as Professor of Chemistry at IIT Delhi. His interests are in the synthesis and properties of materials (dielectric and superconducting oxides, quaternary chalcogenides, polar intermetallics (Zintl phases). He has published over 100 papers in refereed international journals. He has been awarded the *MRSI Medal* for 2006 and the *CRSI Medal* for 2007.